Environmental Science & Technology

pubs.acs.org/est

Article

Radical-Driven Decomposition of Graphitic Carbon Nitride Nanosheets: Light Exposure Matters

Mengqiao Li, Dairong Liu, Xing Chen, Zhihong Yin, Hongchen Shen, Ashlee Aiello, Kevin R. McKenzie, Jr., Nan Jiang, Xue Li, Michael J. Wagner, David P. Durkin,* Hanning Chen,* and Danmeng Shuai*

Cite This: *Environ. Sci. Technol.* 2021, 55, 12414−12423

Read Online

ACCESS | Metrics & More | Article Recommendations | Supporting Information

ABSTRACT: Understanding the transformation of graphitic carbon nitride (g-C_3N_4) is essential to assess nanomaterial robustness and environmental risks. Using an integrated experimental and simulation approach, our work has demonstrated that the photoinduced hole (h^+) on g-C_3N_4 nanosheets significantly enhances nanomaterial decomposition under $^{\bullet}OH$ attack. Two g-C_3N_4 nanosheet samples D and M2 were synthesized, among which M2 had more pores, defects, and edges, and they were subjected to treatments with $^{\bullet}OH$ alone and both $^{\bullet}OH$ and h^+. Both D and M2 were oxidized and released nitrate and soluble organic fragments, and M2 was more susceptible to oxidation. Particularly, h^+ increased the nitrate release rate by 3.37−6.33 times even though the steady-state concentration of $^{\bullet}OH$ was similar. Molecular simulations highlighted that $^{\bullet}OH$ only attacked a limited number of edge-site heptazines on g-C_3N_4 nanosheets and resulted in peripheral etching and slow degradation, whereas h^+ decreased the activation energy barrier of C−N bond breaking between heptazines, shifted the degradation pathway to bulk fragmentation, and thus led to much faster degradation. This discovery not only sheds light on the unique environmental transformation of emerging photoreactive nanomaterials but also provides guidelines for designing robust nanomaterials for engineering applications.

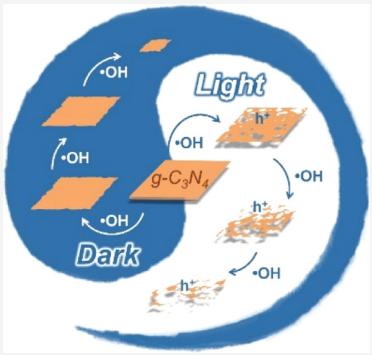

KEYWORDS: *graphitic carbon nitride, nanomaterial aging, photocatalysis, hydroxyl radical, photoinduced hole*

INTRODUCTION

Graphitic carbon nitride (g-C_3N_4), a polymer composed of interconnected *s*-triazines or heptazines,[1] has emerged as a promising engineered nanomaterial (ENM) for diverse applications. In the past decade, nanosized g-C_3N_4 has been extensively used for water treatment, air purification, antimicrobials, energy storage, electronics, sensing, biomedical engineering, and membrane separation,[1−7] owing to its unique 2D nanostructure, excellent photoreactivity under visible light irradiation, remarkable chemical stability and biocompatibility, and affordable cost of manufacture. Researchers have published more than 9000 publications about g-C_3N_4 to date (based on Web of Science, May 2021), and the global market for carbon nitride is expected to steadily grow in the next 5 years.[8] With global production and usage, incidental release and inappropriate disposal of g-C_3N_4 are inevitable, which may raise growing concerns among scientific communities and policy makers, considering the potential adverse environmental and health impacts of this ENM.[9,10] Therefore, it is imperative to evaluate and understand the environmental transformation, fate, and toxicity of g-C_3N_4 to advance regulations and commercial acceptance.[10−12] However, the knowledge about how nanosized g-C_3N_4 persists and ages during engineering applications and in natural aquatic environments is very limited,[5,13,14] and its chemical transformation kinetics and pathway at a molecular level are unknown. $^{\bullet}OH$ is one of the most powerful oxidants (E^0 = 2.8 V), which plays an essential role in the operational aging and environmental transformation of numerous ENMs, including but not limited to silver nanoparticles, carbon dots, carbon nanotubes, graphene, and graphene-like ENMs.[7,14−20] In contrast to some photoreactive ENMs that are highly susceptible to photocorrosion and even oxidation by weak oxidants like O_2 and water,[21−24] g-C_3N_4 was considered to be highly stable and only $^{\bullet}OH$ was responsible for its decomposition.[14] Nevertheless, we found that g-C_3N_4 nanosheets suffered from apparent photocorrosion even though a trace amount of $^{\bullet}OH$ was generated in photocatalysis. This intriguing discovery led us to hypothesize that photoreactivity and h^+ played a critical yet underexplored role in g-C_3N_4 nanomaterial oxidation and transformation. Photoreactive ENMs may involve a distinct mechanism during nanomaterial aging and environmental transformation, in

Received: June 10, 2021
Revised: August 3, 2021
Accepted: August 4, 2021
Published: September 1, 2021

https://doi.org/10.1021/acs.est.1c03804
Environ. Sci. Technol. 2021, 55, 12414−12423

contrast to numerous well-known ENMs that are not photoreactive.

In this study, we leveraged molecular simulations, advanced microscopy and spectroscopy characterizations, and reaction kinetics to understand the molecular mechanism of $^{\bullet}OH$-driven decomposition of g-C_3N_4 nanosheets by taking nanomaterial photoreactivity into account. We fabricated two g-C_3N_4 nanosheets, one showing more pores, defects, and edges compared to the other, and treated them with $^{\bullet}OH$ in the presence or absence of light irradiation. For the first time, the synergy between h^+ and $^{\bullet}OH$ is revealed for the transformation and aging of photoreactive ENMs. In the dark, $^{\bullet}OH$ can only attack a limited number of heptazine units at the edge of g-C_3N_4 nanosheets, leading to slow peripheral etching of the nanosheets. Under light irradiation, the presence of h^+ decreases the activation energy (ΔG_a) of C−N bond breaking between heptazine units in the bulk phase and at edges simultaneously. As a result, fast fragmentation occurs across the whole g-C_3N_4 nanosheets. h^+ not only promotes the degradation kinetics of g-C_3N_4 nanosheets but also diverts the reaction pathway. Our work elucidates fundamental chemistry of the transformation and aging of photoreactive ENMs, provides first insights into their environmental fate and behavior, and inspires the rational design of robust nanomaterials for engineering applications. Our work also has potential broad impacts on understanding the environmental risks and material stability of many other emerging photoreactive ENMs, for example, boron nitride, black phosphorus, transition-metal carbides, (oxy)nitrides, phosphides, aresenides, chalcogenides, and oxyhalides.

MATERIALS AND METHODS

Synthesis of g-C_3N_4 Nanosheets. Sample M2 was synthesized through a top-down post-thermal etching method with modifications.[25] Briefly, bulk g-C_3N_4 powder was first synthesized from melamine by thermal polycondensation and then the powder was thermally exfoliated to produce nanosheets. Sample D was synthesized by using a bottom-up approach based on the literature with modifications.[26] Briefly, melamine was first hydrolyzed in phosphoric acid to produce cyanuric acid, which formed a supramolecule with the remaining melamine. Next, the supramolecule was treated with alcohols for intercalation and thermally polycondensed to produce the nanosheet. More details of used chemicals and material synthesis can be found in Texts S1 and S2 in the Supporting Information, respectively.

Characterization of g-C_3N_4 Nanosheets. The morphological, optical, physical, and chemical properties of fresh and aged g-C_3N_4 nanosheets were characterized. Transmission electron microscopy (TEM), atomic force microscopy (AFM), and scanning tunneling microscopy (STM) were used to characterize the morphology, dimension, and thickness of g-C_3N_4 nanosheets. X-ray powder diffraction (XRD) was used to characterize the crystal structure of the nanosheets. Electrophoretic light scattering was used to evaluate the zeta potential of the nanosheets in an aqueous environment. Bulk contents of carbon, hydrogen, and nitrogen of the nanosheets were quantified using a CHN analyzer. Inductively coupled plasma mass spectrometry (ICP-MS) was used to determine the residual phosphorous species as an impurity in freshly synthesized sample D, and negligible phosphorous was found (<0.06 wt %). Optical absorption spectra of the nanosheets were recorded using a UV−vis spectrophotometer with a diffuse reflectance infrared Fourier transform spectroscopy accessory, and photoluminescence (PL) spectra were obtained from a home-made apparatus based on a rapid-scan Fourier transform infrared spectrometer. The surface area was determined from nitrogen adsorption isotherms using the Brunauer−Emmett−Teller method. The oxidation states and bonding environment of carbon, nitrogen, and oxygen of the nanosheets were characterized by X-ray photoelectron spectroscopy (XPS). Details are in Text S3.

Ozonation, Photocatalytic Ozonation, Peroxonation, and Photocatalytic Peroxonation of g-C_3N_4 Nanosheets. g-C_3N_4 nanosheets were treated and aged by ozonation (O_3 only), photocatalytic ozonation (O_3 and light irradiation), peroxonation (H_2O_2 and O_3), and photocatalytic peroxonation (H_2O_2, O_3, and light irradiation). 180 mg of D or M2 was suspended in 180 mL of ultrapure water (18.25 MΩ cm) and then the 1 g L^{-1} suspension was transferred to a tall borosilicate glass beaker (250 mL) and continuously sparged with O_3 through a gas diffusor in the dark or under light emitting diode (LED) irradiation (7 W, Text S4) for ozonation or photocatalytic ozonation, respectively. Industrial oxygen gas with a flow rate of 0.4 L min^{-1} was used to produce O_3 in an ozone generator (Absolute Ozone NANO), with an O_3 production rate of 4.76 g h^{-1} (99.2 mmol h^{-1}). The steady-state O_3 concentration in suspensions remained at 17 mg L^{-1} (or 0.354 mM, Text S5). For the same setup, 30 wt % H_2O_2 solution was continuously amended into (5.05 mL h^{-1}) the suspensions together with O_3 in the dark or under LED irradiation (7 W) to enable peroxonation or photocatalytic peroxonation, respectively. The feeding rate of H_2O_2 was 49.5 mmol h^{-1}, and the molar ratio of fed H_2O_2 and fed O_3 was kept at 0.5. To prevent interference from other constituents in water, no buffer was used for aging g-C_3N_4 nanosheets but suspension pH was continuously monitored. An aluminum foil and a Parafilm sheet were used to cover the beaker opening to reduce gas leakage and water evaporation during a long-term aging study. Light irradiation was introduced from the side of the beaker, and the borosilicate glass showed negligible absorption of photons with wavelengths of 395, 455, and 525 nm. Detailed characterizations of LED light sources are shown in Figure S1.

The treated g-C_3N_4 nanosheets were collected by ultracentrifugation at 30,000 rpm (108,860*g*, Beckman JXN30), and supernatants were next filtered with 0.2 μm polyvinylidene difluoride (PVDF) syringe filters for analyzing released ions and soluble organics. All experiments were performed with at least three independent replicates.

Nitrogen Release Quantification. The concentration of released nitrite and nitrate in the filtered supernatants after g-C_3N_4 nanosheet aging was analyzed by ion chromatography (Dionex ICS-1100; Dionex IonPac AS18 column) using 18 mM NaOH as the eluent and 0.25 mL min^{-1} as the eluent flow rate.

Organic Release Quantification. The concentration of released soluble organic compounds in the filtered supernatants after g-C_3N_4 nanosheet aging was analyzed using a total organic carbon (TOC) analyzer (Shimadzu TOC-VCP) and a high-resolution quadrupole Orbitrap mass spectrometer. Details are in Text S6.

Hydroxyl Radical Concentration Measurement. 4-chlorobenzoic acid (*p*-CBA) was used as the probe compound for quantifying steady-state $^{\bullet}OH$ concentrations ($[^{\bullet}OH]_{ss}$) because the reaction between *p*-CBA and $^{\bullet}OH$ is highly

https://doi.org/10.1021/acs.est.1c03804
Environ. Sci. Technol. 2021, 55, 12414−12423

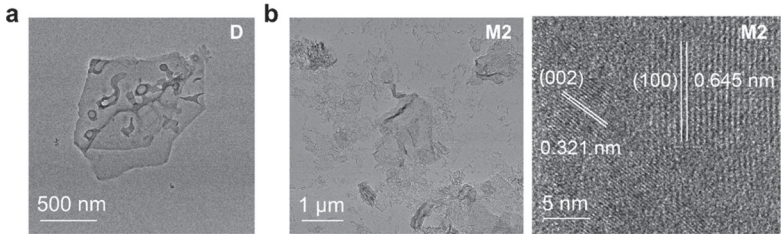

Figure 1. Morphological characterization of fresh g-C_3N_4 nanosheets. TEM of fresh D (a), TEM (b left) and high-resolution TEM (b right) of fresh M2.

selective and fast. During ozonation, photocatalytic ozonation, peroxonation, and photocatalytic peroxonation, 20 μM of *p*-CBA was introduced into the suspensions when g-C_3N_4 nanosheets were aged for 1 h and then the suspensions (0.5 mL) were sampled at different time intervals after *p*-CBA amendment (every 5 or 10 s) and residual oxidants were quenched by adding $Na_2S_2O_3$ (200 mM and 40 μL) immediately. *p*-CBA amendment, sample collection, and oxidant quenching were repeated when g-C_3N_4 nanosheets were aged for 3, 5, and 7 h, respectively. Centrifugation (13,000 rpm and 16,060*g*) or filtration (PVDF syringe filters with a pore size of 0.2 μm) was used to harvest the liquid for *p*-CBA quantification by high performance liquid chromatography (HPLC, Text S7). $[^{\bullet}OH]_{ss}$ was calculated using the following equation:[27]

$$[^{\bullet}OH]_{ss} = \frac{k_{ex}}{k_{p\text{-CBA}/^{\bullet}OH}} = \frac{\ln\left(\frac{[p\text{-CBA}]_0}{[p\text{-CBA}]_t}\right)/t}{k_{p\text{-CBA}/^{\bullet}OH}} \quad (1)$$

where k_{ex} refers to the experimentally determined pseudo-first-order reaction rate constant of *p*-CBA, $k_{p\text{-CBA}/^{\bullet}OH}$ is the second-order reaction rate constant between *p*-CBA and $^{\bullet}OH$ (5.2×10^9 M^{-1} s^{-1}), and $[p\text{-CBA}]_0$, $[p\text{-CBA}]_t$, and t represent initial *p*-CBA concentration, *p*-CBA concentration at time t, and sampling time, respectively. The average $[^{\bullet}OH]_{ss}$ was reported from the values calculated at 1, 3, 5, and 7 h of the reaction. Detailed parameters of HPLC analysis can be found in Table S1. Selection of *p*-CBA with an initial concentration of 20 μM for $[^{\bullet}OH]_{ss}$ quantification is justified in Text S8, and the lifetime of $^{\bullet}OH$ was estimated as 0.18 μs in ozonation, photocatalytic ozonation, peroxonation, and photocatalytic peroxonation (Text S9). All experiments were performed with at least three independent replicates.

Because there was no buffer in our systems, pH of reaction suspensions dropped to ~3 during the reaction. Particularly, in photocatalytic ozonation, under the irradiation of a 395 nm LED lamp, pH of the suspensions containing D and M2 immediately dropped from 7.8 to 4.4 and 3.9 in 10 min, respectively, and it gradually leveled off (pH of D suspension was 4.2 and 3.4 after 1 and 8 h treatment, respectively; pH of M2 suspension was 3.4 and 2.8 after 1 and 8 h treatment, respectively). The quantification of $[^{\bullet}OH]_{ss}$ was not expected to be influenced[28−30] because pH remained almost the same after 1 h of reaction, when the first measurement for $[^{\bullet}OH]_{ss}$ was conducted. Indeed, the difference in $[^{\bullet}OH]_{ss}$ at 1, 3, 5, and 7 h during photocatalytic ozonation and ozonation was statistically insignificant (Figure S2).

p-CBA could adsorb on the surface of g-C_3N_4 nanosheets with its carboxyl group, similar to its adsorption to many other carbon-based materials and thus quantifies both near-surface and bulk-phase $^{\bullet}OH$.[31−33] In addition, ozonation and photocatalytic ozonation on g-C_3N_4 mainly produces bulk-phase but not near-surface $^{\bullet}OH$ as the dominant reactive species likely due to rapid desorption and diffusion of $^{\bullet}OH$ from the g-C_3N_4 surface.[34] Therefore, *p*-CBA can accurately quantify $^{\bullet}OH$ production in our systems during the aging of g-C_3N_4 nanosheets.

Computational Simulation. In the computational study for understanding C−N bond breaking, bulk-phase g-C_3N_4 was represented by a 6 × 6 supercell of heptazine units connected by tertiary amines (Figure S3a), whereas the edge moieties of g-C_3N_4 are terminated by either primary or secondary amines (Figure S3b). Unless otherwise specified, all of our simulations were performed using CP2K,[35] an open-source software, with Goedecker−Teter−Hutter pseudopotential,[36] the Heyd−Scuseria−Ernzerhof hybrid (HSE06) exchange−correlation function,[26,37] a polarized-valence-double-zeta basis set,[38] and a wavelet-based Poisson solver.[39] It has been found that the chemical bond formed between the tertiary nitrogen atom and the corner carbon atom of heptazine units has a dissociation energy of ~90 kcal mol^{-1}, which is at least 20 kcal mol^{-1} lower than that of any other chemical bond in g-C_3N_4. Therefore, our discussion on C−N bond breaking focused on the bond between the tertiary nitrogen atom and the corner carbon atom of the heptazine units. More details of the simulation can be found in Text S10.

RESULTS AND DISCUSSION

Synthesis and Characterization of Fresh g-C_3N_4 Nanosheets. Two types of few-layered g-C_3N_4 nanosheets were synthesized to explore their decomposition, which represent typical g-C_3N_4 nanomaterials for a broad range of future applications. Specifically, sample D (Figure 1a) was fabricated by using a bottom-up approach, that is, thermal polycondensation of melamine-cyanuric acid supramolecules after ethanol and glycerol intercalation.[26] Sample M2 (Figure 1b left) was thermally exfoliated from bulk g-C_3N_4 powders using a top-down strategy.[25] D had a more well-defined structure than M2, but their lateral sizes were similar, that is, around several hundreds of nanometers to a couple of micrometers. The thickness of D and M2 was 3−5 and 5−10 nm, respectively, as characterized by AFM (Figure S4a,b). Notably, nanosheets with an average height of 2.2 Å were observed by STM for characterizing M2, and the height was consistent with the thickness of single-layer g-C_3N_4 (Figure S4c).[40] To confirm that the nanosheets were g-C_3N_4 instead of the Au substrate used in sample characterization, the conductivity was measured. The nonlinear I−V curve underscored the semiconductor nature of g-C_3N_4 (Figure S4d), in contrast to Au showing a linear *I*−*V* curve. STM indicated single-layer g-C_3N_4 nanosheets did exist in our samples. The specific surface area of D and M2 was

https://doi.org/10.1021/acs.est.1c03804
Environ. Sci. Technol. 2021, 55, 12414−12423

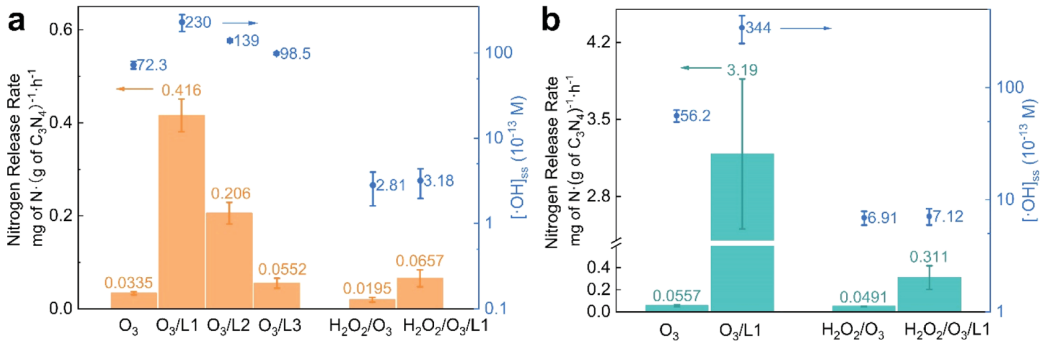

Figure 2. Aging of g-C_3N_4 nanosheets. NRR for D (a) and M2 (b) in 8 h ozonation (O_3), photocatalytic ozonation (O_3/L1, O_3/L2, and O_3/L3), peroxonation (H_2O_2/O_3), and photocatalytic peroxonation (H_2O_2/O_3/L1). The average steady-state hydroxyl radical concentrations ($[^{\bullet}OH]_{ss}$) throughout 8 h treatment are shown on the right *y* axis. L1, L2, and L3 refer to LED irradiation of 395, 455, and 525 nm, respectively. The aging condition of g-C_3N_4 nanosheets are as follows: a nanosheet loading of 1 g L^{-1}, no buffer, a steady-state O_3 concentration of 17.0 mg L^{-1} (0.354 mM) for ozonation and photocatalytic ozonation, and continuous feeding of 30 wt % H_2O_2 at 5.05 mL h^{-1} beyond O_3 for peroxonation and photocatalytic peroxonation. All experiments were conducted in triplicate, and the error bars represent average value ± standard deviation.

determined as 21.6 ± 3.4 and 168 ± 1 m^2 g^{-1}, respectively, and thus, M2 had more active sites in photocatalysis (Figure S5). Indeed, the photocatalytic activity of M2 for phenol (PHE) degradation was 2.33−2.70 times higher than that of D (Figure S6). Type IV nitrogen adsorption isotherms suggested the existence of pores in both g-C_3N_4 nanosheet samples, which was consistent with the TEM characterization. Moreover, M2 had a much higher PL intensity than D (Figure S7), and the result indicated that M2 had more defects to promote radiative recombination of charge carriers. The XRD patterns (Figure S8) suggested that both D and M2 were crystalline, and they were g-C_3N_4. The main peak at 2θ = 27.9° referred to the (002) plane of the layered graphitic structure with a *d*-spacing of 0.326 nm while the weaker peak at 13.0° stemmed from the intralayer packing of the (100) plane with a *d*-spacing of 0.680 nm,[26] which was consistent with the high-resolution TEM of M2 (Figure 1b right). Bulk composition analysis also confirmed that both samples were g-C_3N_4 (carbon to nitrogen weight ratio of 0.574 and 0.582 for D and M2, respectively). In summary, these morphological, physical, chemical, and optical characterizations all suggested that M2 had more pores, defects, and edges and was more photoreactive than D, highlighting that M2 could be more susceptible to oxidation.

g-C_3N_4 Nanosheet Decomposition with the Synergy between $^{\bullet}OH$ and h^+. $^{\bullet}OH$ is ubiquitous in natural environments and engineering settings, and it plays a critical role in determining the stability, transformation, fate, and environmental and health impacts of ENMs.[14−20] A previous study demonstrated the excellent stability of g-C_3N_4 even under the attack of high concentrations of O_3 and $^{\bullet}O_2^-$, but the material decomposed in the presence of $^{\bullet}OH$.[14] We used a continuous feed of O_3 to create a steady-state concentration of $^{\bullet}OH$ on the order 10^{-12} M ($[^{\bullet}OH]_{ss}$, Figure 2a,b), which was in the similar range of many advanced oxidation processes.[28−30,41−44] After continuous oxidation with $^{\bullet}OH$, D and M2 were oxidized and decomposed. Nitrate but not nitrite was observed in the aqueous phase after oxidizing g-C_3N_4 nanosheets, and soluble organic fragments including cyameluric acid were also released (Figure S9 and Table S2). The byproducts, that is, nitrate and cyameluric acid, were also confirmed in a previous study.[14] To elucidate the mechanism and identify the role of photocatalysis in g-C_3N_4 nanosheet decomposition, we used LED lamps that irradiated photons at 395 nm (L1), 455 nm (L2), and 525 nm (L3) to excite the g-C_3N_4 nanosheets. In these experiments (O_3/L1, O_3/L2, and O_3/L3), O_3 was unable to be excited because of negligible light absorption at these wavelengths (Text S4 and Table S3). h^+ on g-C_3N_4 also did not have sufficient energy to oxidize water to $^{\bullet}OH$ because of the less-positive valence band of g-C_3N_4 compared to the reduction potential of $^{\bullet}OH/H_2O$ (Table S4).[45,46] Instead, O_3 molecules captured photoinduced electrons efficiently to enhance $^{\bullet}OH$ generation through a one-electron reduction pathway ($O_3 \rightarrow {}^{\bullet}O_3^- \rightarrow HO_3^{\bullet} \rightarrow {}^{\bullet}OH$).[41]

In comparison to ozonation, $[^{\bullet}OH]_{ss}$ in O_3/L1 was significantly enhanced by 3.18 and 6.12 times for D and M2, respectively. M2 enabled more $^{\bullet}OH$ generation due to its higher photoreactivity. Moreover, $[^{\bullet}OH]_{ss}$ in photocatalytic ozonation of D increased under the irradiation of L3 to L2 to L1, which was in line with the light absorbance and photoreactivity of D (Figure S5). Enhanced photoreactivity could promote $^{\bullet}OH$ production via the reduction of O_3.[41] No apparent morphological change for both g-C_3N_4 nanosheet samples was observed even after 24 h of O_3/L1 (Figure S10a,b). However, both samples showed an increased surface oxygen content and surface charge negativity based on XPS and zeta potential analysis, respectively, indicating that oxidation occurred and functional groups such as −OH or −COOH might be introduced on the surface. For example, surface oxygen content in atomic percentage (at %) increased from 3.60 to 6.80% for D and from 1.00 to 7.80% for M2 after 24 h of O_3/L1, respectively (Figure S11 and Table S5), while the zeta potential decreased from −42.7 to −62.5 mV for D and from −32.0 to −45.8 mV for M2 under the same treatment condition, respectively. In contrast, ozonation did not increase surface oxygen content (3.60 vs 3.40 at % for D before and after ozonation) and only moderately decreased the zeta potential (−42.7 vs −48.3 mV for D before and after ozonation). Compared to ozonation, photocatalytic ozonation of both g-C_3N_4 nanosheets generally produced more nitrate and more soluble organic fragments including cyameluric acid as the oxidation byproducts. For example, on comparing O_3/L1 with ozonation, D released 3.96 and 11.6 times more total organic carbon and cyameluric acid, respectively (Figure S12 and Table S2). Similar to $^{\bullet}OH$ production, the amount of released nitrate and organic byproducts was also positively correlated with the photoreactivity of g-C_3N_4 nanosheets.

https://doi.org/10.1021/acs.est.1c03804
Environ. Sci. Technol. 2021, 55, 12414−12423

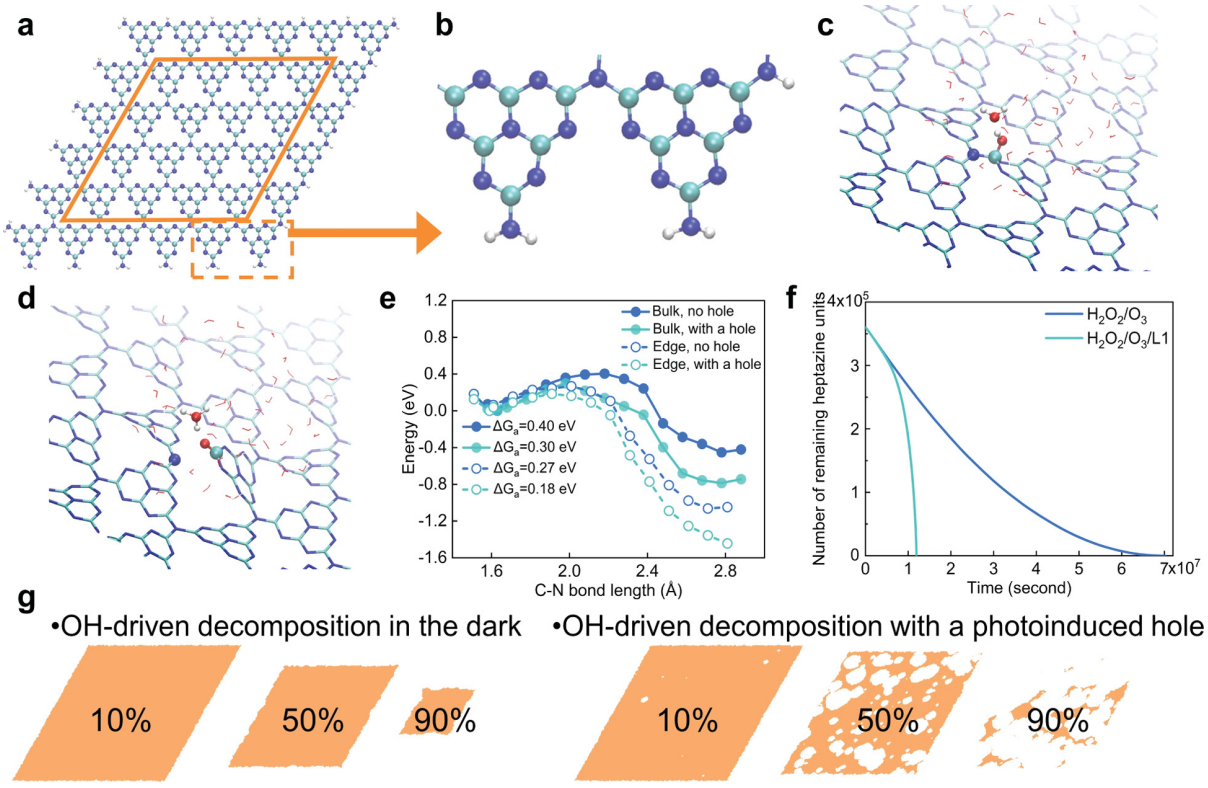

Figure 3. Molecular simulation of g-C_3N_4 nanosheet aging. A g-C_3N_4 nanosheet (a) consisting of 6 × 6 heptazine units with the highlighted bulk phase (solid parallelogram) and edge sites (dash rectangular). Two edge-site heptazine units are also shown in (b). Optimized g-C_3N_4/•OH adduct solvated in water (c) before and (d) after C−N bond breaking. For visual clearance, only the H_2O forming a hydrogen bond with the •OH is highlighted whereas other water molecules are intentionally blurred. (e) Calculated energy profile as a function of the C−N bond length for a bulk-phase or edge-site heptazine unit, treated under the dark conditions with no h^+ and light exposure with one hole, respectively. (f) Simulated number of remaining heptazine units as a function of aging time for D during peroxonation and photocatalytic peroxonation (H_2O_2/O_3 and H_2O_2/O_3/L1). (g) Visualization of g-C_3N_4 nanosheet decomposition during peroxonation and photocatalytic peroxonation. 10, 50, and 90% degradation of g-C_3N_4 nanosheets indicates the number of decomposed heptazine units to the number of total heptazine units in the nanosheets. White, red, cyan, and blue balls in the structures refer to hydrogen, oxygen, carbon, and nitrogen atoms, respectively.

During O_3/L1, M2 released 7.67 times more nitrate and 1.26 times more cyameluric acid compared to D (Figure 2a,b, and Table S2), which suggests that M2 with more pores, defects, and edges and higher photoreactivity was prone to degradation. Cyameluric acid production in photocatalytic ozonation of D also increased under the irradiation of L3 to L2 to L1 (Table S2). We used the nitrogen release rate (NRR), that is, nitrate-nitrogen released per unit mass of g-C_3N_4 nanosheets per unit time, as a decomposition rate indicator, which was also confirmed as a valid parameter to characterize g-C_3N_4 aging in ozonation and photocatalytic ozonation based on a previous study.[14] Surprisingly, NRR enhancement was disproportionately larger than the $[^{\bullet}OH]_{ss}$ increase in photocatalytic ozonation versus ozonation. On comparing O_3/L1 with ozonation of D, $[^{\bullet}OH]_{ss}$ and NRR increased by 3.18- and 12.4-fold, respectively. NRR was also dramatically promoted by 57.3-fold for treating M2 when O_3/L1 was compared to ozonation, whereas $[^{\bullet}OH]_{ss}$ increased by merely 6.12-fold (Figure 2a,b). In addition, M2 released 7.67 times more nitrate than D in O_3/L1, despite the fact that $[^{\bullet}OH]_{ss}$ slightly increased by 49.6% (Figure 2b). Moreover, control experiments indicated that NRR of both nanosheets was negligible in the dark, either without O_3 or only with H_2O_2 treatment, while photocatalysis alone decomposed the nanosheets and produced a remarkable amount of nitrate (Table S4). All these results highlighted that other unknown key factors beyond •OH determined the decomposition of g-C_3N_4 nanosheets and they could be associated with the photoreactivity of the nanomaterial.

Peroxonation, the treatment coupling H_2O_2 with O_3, was commonly used for water purification due to a much higher •OH formation rate (reaction R1) than that from O_3 decomposition (reactions R2 and R3).[47]

$$2O_3 + H_2O_2 \rightarrow 2^{\bullet}OH + 3O_2 \quad (R1)$$

$$3O_3 + OH^- \rightarrow {}^{\bullet}OH + O_3^{\bullet -} + 3O_2 \quad (R2)$$

$$O_3^{\bullet -} + H^+ \leftrightarrow HO_3^{\bullet} \leftrightarrow {}^{\bullet}OH + O_2 \quad (pH < 8) \quad (R3)$$

$$O_3 + {}^{\bullet}OH \rightarrow HO_2^{\bullet} + O_2 \quad (R4)$$

$$H_2O_2 + {}^{\bullet}OH \rightarrow HO_2^{\bullet} + H_2O \quad (R5)$$

The •OH generation efficiency highly depends on the molar ratio of H_2O_2 to O_3 because excessive O_3 and H_2O_2 can also quench •OH through reactions R4 and R5.[47−49] Because H_2O_2 and byproducts of R4 and R5 (i.e., O_2 and $HO_2^{\bullet}$) do not oxidize and degrade g-C_3N_4,[14] introducing H_2O_2 together with O_3 can generate a clean system for g-C_3N_4 aging and it can easily tailor $[^{\bullet}OH]_{ss}$. On comparing peroxonation with ozonation, $[^{\bullet}OH]_{ss}$ decreased by 96.1 and 87.7% for treating

https://doi.org/10.1021/acs.est.1c03804
Environ. Sci. Technol. 2021, 55, 12414−12423

D and M2, respectively, likely due to the presence of excessive oxidants for scavenging •OH. However, NRR only decreased by 41.8% and 11.8% for treating D and M2, respectively (Figure 2a,b). Therefore, a high $[^{\bullet}OH]_{ss}$ does not necessarily translate into a proportionally increased decomposition rate of the g-C_3N_4 nanosheets because only a limited number of g-C_3N_4 sites might be attacked and oxidized by •OH. On comparing peroxonation and photocatalytic peroxonation (H_2O_2/O_3/L1) of D, even though $[^{\bullet}OH]_{ss}$ was similar, NRR under light exposure was 3.37 times higher than that in the dark. M2 also released 6.33 times more nitrate in H_2O_2/O_3/L1 than in peroxonation when $[^{\bullet}OH]_{ss}$ in both treatment processes was statistically the same. The results clearly demonstrated that the photoreactivity of g-C_3N_4 nanosheets played a critical role in nanomaterial decomposition.

Mechanism of g-C_3N_4 Nanosheet Decomposition. We hypothesized that h^+ promoted g-C_3N_4 nanosheet decomposition under •OH attack, and Monte Carlo simulations were carried out using parameters derived from transition-state theory for testing the hypothesis. The C−N bond between heptazine units (Figure 3a,b) has the lowest bond dissociation energy and is thus most vulnerable to •OH oxidation. An electron-deficient •OH can launch an electrophilic attack on one of the three corner carbon atoms of a triangular heptazine unit to form a C−O single bond (Figure 3c). Because oxygen is even more electronegative than nitrogen, the C−N single bond between the attacked corner carbon atom and the tertiary nitrogen atom is expected to be weakened through electron transfer, eventually leading to bond breaking and nanosheet decomposition (Figure 3d). Without light irradiation, the calculated ΔG_a for C−N bond breaking under •OH attack of edge-site and bulk-phase heptazine was 0.27 and 0.40 eV, respectively (Figure 3e, edge-site and bulk-phase heptazine units are highlighted in Figure 3a,b). This remarkable difference in ΔG_a made the edge sites of g-C_3N_4 nanosheets much more susceptible to •OH attack in the dark, and the limited number of edge sites led to a negligible difference in NRR in ozonation and peroxonation. Importantly, the presence of h^+ decreased ΔG_a from 0.40 to 0.30 eV for the bulk-phase C−N bond breaking and from 0.27 to 0.18 eV for the edge-site C−N bond breaking (Figure 3e), speeding up the reaction rate from 1 μs^{-1} to 10 ns^{-1} (Table S6). Meanwhile, the h^+ drastically increased ΔG_a for C−N bond reformation, further accelerating g-C_3N_4 decomposition. Because the typical lifetime of photoexcited g-C_3N_4 is on the nanosecond timescale[26] that is much shorter than our calculated time for C−N bond breaking, our proposed mechanism of g-C_3N_4 decomposition is in sharp contrast to that of photoinduced water oxidation, wherein its sub-nanosecond reaction primarily proceeds on the excited-state potential energy surface.[50,51] Moreover, in light of the rich presence of •OH, O_3, O_2, and/or H_2O_2 in our aqueous solutions, the heptazinyl radicals reported in studies of water oxidation[52,53] are unlikely to materialize for g-C_3N_4 decomposition, making the h^+-induced C−N bond breaking a more feasible reaction pathway.

In our Monte Carlo protocol, the identity of each heptazine unit was recorded once it was removed so that the whole decomposition process was tracked over time to the finest resolution. Aiming to examine the effect of light exposure on g-C_3N_4 nanosheet decomposition, we investigated peroxonation and H_2O_2/O_3/L1 treatment of D (Table S7), for their similar $[^{\bullet}OH]_{ss}$ yet distinct NRR. The initial size of each sample was 600 × 600 heptazine units that was equivalent to 430 nm × 430 nm, a typical lateral size of D. To ensure statistical reliability, each curve in Figure 3f was averaged over 100 Monte Carlo trajectories, diminishing the standard deviation of our simulated aging rates to ±0.001 s^{-1}. Although our fabricated g-C_3N_4 nanosheets are intrinsically defective with a large number of pores, the simulations on the initially defect-free samples are still informative by showing qualitatively sensible trends of C−N bond breaking. As shown in Figure 3f, D decomposition during H_2O_2/O_3/L1 was substantially faster compared to peroxonation, and the highest decomposition rate in H_2O_2/O_3/L1 was 3.50 times larger than that in peroxonation (0.0420 vs 0.0120 s^{-1}). More interestingly, the presence of h^+ changes the pathway of g-C_3N_4 nanosheet decomposition (Figure 3g). Nanosheet degradation takes place mainly at edge sites under the attack of only •OH (peripheral etching). In contrast, the synergy between •OH and h^+ leads to nanosheet degradation from both edges and the bulk (fragmentation). The simulation result is also supported by the fact that a significant amount of oxygen was introduced to g-C_3N_4 nanosheets only after O_3/L1 but not ozonation (Figure S11 and Table S5).

Photocatalytic Performance of Fresh and Aged g-C_3N_4 Nanosheets. We are interested in knowing how the photoreactivity of g-C_3N_4 nanosheets changes after aging because the research outcomes can not only highlight nanomaterial robustness in engineering systems but also shed light on the long-term ecological impacts of the nanomaterials once they are released into the environment. Four organic contaminants, namely, PHE, sulfamethoxazole (SMX), atrazine (ATZ), and carbamazepine (CBZ), were used for evaluating the photocatalytic performance of both fresh and aged g-C_3N_4 nanosheets (Text S11). These contaminants were selected because of their diverse chemical structures and properties, broad industrial, agricultural, and biomedical applications, and persistence in the environment.[54,55] Photocatalytic activity of g-C_3N_4 nanosheets for degrading the organic contaminants varied along with nanomaterial aging (Figure 4). In general, compared to fresh g-C_3N_4 nanosheets, ozonation-treated samples showed comparable or better photocatalytic activity for degrading all selected contaminants, except for using M2 for SMX degradation. In contrast, almost all g-C_3N_4 nano-

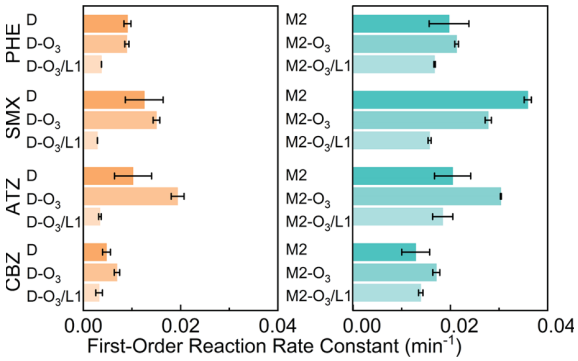

Figure 4. Photoreactivity of fresh and aged g-C_3N_4 nanosheets for contaminant degradation. PHE, SMX, ATZ, and CBZ refer to phenol, sulfamethoxazole, atrazine, and carbamazepine, respectively. Photocatalytic contaminant degradation tests were conducted under the following conditions: a 1000 W xenon lamp with an AM 1.5G optical filter, a nanosheet loading of 0.2 g L^{-1}, an initial contaminant concentration of 50 μM, and phosphate buffer of 1 mM (pH 7).

https://doi.org/10.1021/acs.est.1c03804
Environ. Sci. Technol. 2021, 55, 12414−12423

sheets treated after photocatalytic ozonation (O_3/L1) showed reduced photoreactivity for contaminant degradation. Gentle oxidation by ozonation could improve the photoreactivity of g-C_3N_4 nanosheets, but extensive nanomaterial degradation and disintegration after photocatalytic ozonation could impair their reactivity. Our study provides the first insight into g-C_3N_4 nanosheet aging and its impact on photoreactivity, and holistic future work is needed to evaluate the production of reactive oxygen species, contaminant−photocatalyst interactions, and the structure−activity relationship of contaminants in photocatalysis for both fresh and aged photoreactive ENMs.

Environmental Implications. Because the co-existence of $^{\bullet}OH$ and h^+ is quite common in photocatalysis,[41−44] our research first highlights the need for developing robust photoreactive ENMs for catalytic applications. As a visible-light-responsive photocatalyst, g-C_3N_4 holds promise for water purification and disinfection, renewable energy production, and value-added chemical synthesis,[1−3] with the prerequisite that the material maintains its performance in long-term reactions. However, the photoreactivity of g-C_3N_4 nanosheets varied along with the nanomaterial aging, which calls for an urgent need for fabricating robust ENMs. In addition, M2, the one showing a better photocatalytic activity than D even after aging, decomposed faster and released more undesired byproducts that may induce secondary pollution during applications. The intrinsic high photoreactivity of g-C_3N_4 nanosheets could significantly harm the integrity and long-term activity of this photoreactive ENM, which creates a dilemma. By elucidating the importance of h^+ in g-C_3N_4 decomposition, several strategies are recommended to enhance the longevity of g-C_3N_4. For example, we can construct a *Z*-scheme structure of g-C_3N_4 with another semiconductor, and the h^+ on g-C_3N_4 can be neutralized by the photoinduced electrons of that semiconductor. By doing this, we not only improve photocatalytic performance but also extend the lifetime of g-C_3N_4. This strategy can also be used to protect a broad spectrum of other photoreactive ENMs with lower stability in a multi-component photocatalytic system. In addition, g-C_3N_4 photostability could be improved via physical separation of $^{\bullet}OH$ and h^+ during the reaction. Most g-C_3N_4 samples are not able to produce $^{\bullet}OH$ via h^+ oxidation of water due to a lower energy level of the valence band of g-C_3N_4 compared to the reduction potential of $^{\bullet}OH/H_2O$.[56,57] However, g-C_3N_4 can produce $^{\bullet}OH$ via sequential reduction and protonation of O_2 by photoinduced electrons in the conduction band of g-C_3N_4 and protons near the material. Building a photoelectrocatalytic system with g-C_3N_4 as the photoanode could physically avoid the co-existence of $^{\bullet}OH$ and h^+ on/near g-C_3N_4, that is, h^+ and $^{\bullet}OH$ are generated on the anode and cathode, respectively, which increases the longevity of g-C_3N_4. Prior to engineering applications, a thorough study of photocatalytic performance and ENM stability is recommended.

Our research also highlights how greater attention should be paid to the unique environmental transformation and fate of photoreactive ENMs, which is distinct from non-photoreactive ENMs. $^{\bullet}OH$ is ubiquitous in natural environments and can be produced by the photolysis of nitrite, nitrate, and dissolved organic matter and photo-Fenton reactions in an aquatic environment.[58] The photochemical formation rate of $^{\bullet}OH$ in sunlit freshwater and seawater is on the order of 10^{-7} and 10^{-8} M h^{-1}, respectively, with a steady-state concentration of 10^{-16} and 10^{-18} M, respectively.[58−60] In addition, microbial activities and overturn-induced aeration of anoxic bottom water can produce $^{\bullet}OH$ in the dark, and the amount of generated $^{\bullet}OH$ may be comparable with that of photochemical processes in some waterbodies.[61−63] Even though the amount of $^{\bullet}OH$ produced in natural environments is extremely low compared to our aging systems (10^{-1} M h^{-1}, Text S8), the cumulative effect of $^{\bullet}OH$ cannot be ignored for the long-term decomposition of g-C_3N_4. Due to the excellent properties of g-C_3N_4, the mass production and broad application of the nanomaterial is expected in the foreseeable future, and its release into natural aquatic environments is inevitable. Once released, g-C_3N_4 may undergo photo-accelerated fragmentation under light exposure (e.g., daytime in shallow water) but slow oxidation in the dark (e.g., nighttime, deep water, or in the sediments), both attacked by $^{\bullet}OH$. g-C_3N_4 nanosheets morphology and properties may also be different after aging with and without light exposure, which could determine distinct adverse impacts of the nanomaterial on ecological systems and human health. In addition, the nitrate and soluble organic fragments released during aging may also pose adverse impacts on humans and other organisms.

■ ASSOCIATED CONTENT

Supporting Information

The Supporting Information is available free of charge at https://pubs.acs.org/doi/10.1021/acs.est.1c03804.

Experimental and simulation details; the spectra of light source; composition, band gap, XRD, photoreactivity, zeta potential, and XPS of g-C_3N_4 nanosheets; hydroxyl radical concentration during aging; TOC, cyameluric acid, and nitrogen release from g-C_3N_4 nanosheets during aging (PDF).

■ AUTHOR INFORMATION

Corresponding Authors

David P. Durkin − *Department of Chemistry, United States Naval Academy, Annapolis, Maryland 21402, United States;* orcid.org/0000-0001-5979-8449; Phone: 410-293-6601; Email: durkin@usna.edu; Fax: 410-293-2218

Hanning Chen − *Department of Chemistry, American University, Washington, District of Columbia 20016, United States;* orcid.org/0000-0003-3568-8039; Phone: 202-885-1750; Email: hchen@american.edu; Fax: 202-885-1752

Danmeng Shuai − *Department of Civil and Environmental Engineering, The George Washington University, Washington, District of Columbia 20052, United States;* orcid.org/0000-0003-3817-4092; Phone: 202-994-0506; Email: danmengshuai@gwu.edu; Fax: 202-994-0127; http://materwatersus.weebly.com/

Authors

Mengqiao Li − *Department of Civil and Environmental Engineering, The George Washington University, Washington, District of Columbia 20052, United States;* Present Address: https://mengqiaoli.github.io/

Dairong Liu − *Department of Chemistry, University of Illinois at Chicago, Chicago, Illinois 60607, United States;* orcid.org/0000-0002-9569-8207

Xing Chen − *Institute of Mass Spectrometry and Atmospheric Environment, Jinan University, Guangzhou, Guangdong 510632, P. R. China*

https://doi.org/10.1021/acs.est.1c03804
Environ. Sci. Technol. 2021, 55, 12414−12423

Zhihong Yin − *Institute of Mass Spectrometry and Atmospheric Environment, Jinan University, Guangzhou, Guangdong 510632, P. R. China*
Hongchen Shen − *Department of Civil and Environmental Engineering, The George Washington University, Washington, District of Columbia 20052, United States*
Ashlee Aiello − *Department of Chemistry, United States Naval Academy, Annapolis, Maryland 21402, United States*
Kevin R. McKenzie, Jr. − *Department of Chemistry, The George Washington University, Washington, District of Columbia 20052, United States;* orcid.org/0000-0001-7483-3468
Nan Jiang − *Department of Chemistry, University of Illinois at Chicago, Chicago, Illinois 60607, United States;* orcid.org/0000-0002-4570-180X
Xue Li − *Institute of Mass Spectrometry and Atmospheric Environment, Jinan University, Guangzhou, Guangdong 510632, P. R. China;* orcid.org/0000-0001-9247-0584
Michael J. Wagner − *Department of Chemistry, The George Washington University, Washington, District of Columbia 20052, United States;* orcid.org/0000-0001-9559-7804

Complete contact information is available at: https://pubs.acs.org/10.1021/acs.est.1c03804

Notes

The authors declare no competing financial interest.

■ ACKNOWLEDGMENTS

We acknowledge NSF Grants CHE-1807617 and CHE-1807465 for supporting our study. We also acknowledge the Air Force Office of Scientific Research (MIPR# F4FGA08354G001) and the United States Naval Academy for facilities support. Computational resources were provided by the Argonne Leadership Computing Facilities at Argonne National Laboratory under the Department of Energy contract DE-AC-06CH11357 and by the Extreme Science and Engineering Discovery Environment at Texas Advanced Computing Center under the National Science Foundation contract TG-CHE130008. We thank Elizabeth Eves and Dr. Julio A. N. T. Soares at the University of Illinois at Urbana-Champaign for CHN, ICP-MS, band gap, and PL analyses and Dr. Zhiwu Wang and Jody Smiley at Virginia Tech for the TOC analysis.

■ REFERENCES

(1) Hao, Q.; Jia, G.; Wei, W.; Vinu, A.; Wang, Y.; Arandiyan, H.; Ni, B.-J. Graphitic Carbon Nitride with Different Dimensionalities for Energy and Environmental Applications. *Nano Res.* **2020**, *13*, 18−37.
(2) Volokh, M.; Peng, G.; Barrio, J.; Shalom, M. Carbon Nitride Materials for Water Splitting Photoelectrochemical Cells. *Angew. Chem., Int. Ed.* **2019**, *58*, 6138−6151.
(3) Zhang, C.; Li, Y.; Shuai, D.; Shen, Y.; Xiong, W.; Wang, L. Graphitic Carbon Nitride ($g\text{-}C_3N_4$)-Based Photocatalysts for Water Disinfection and Microbial Control: A Review. *Chemosphere* **2019**, *214*, 462−479.
(4) Liu, J.; Wang, H.; Antonietti, M. Graphitic Carbon Nitride "Reloaded": Emerging Applications beyond (Photo)Catalysis. *Chem. Soc. Rev.* **2016**, *45*, 2308−2326.
(5) Sano, T.; Tsutsui, S.; Koike, K.; Hirakawa, T.; Teramoto, Y.; Negishi, N.; Takeuchi, K. Activation of Graphitic Carbon Nitride ($g\text{-}C_3N_4$) by Alkaline Hydrothermal Treatment for Photocatalytic NO Oxidation in Gas Phase. *J. Mater. Chem. A* **2013**, *1*, 6489.
(6) Aquino de Carvalho, N.; Wang, Y.; Morales-Soto, N.; Waldeck, D.; Bibby, K.; Doudrick, K.; Gilbertson, L. M. Using C-Doping to Identify Photocatalytic Properties of Graphitic Carbon Nitride That Govern Antibacterial Efficacy. *ACS ES&T Water* **2021**, *1*, 269−280.
(7) Shen, H.; López-Guerra, E. A.; Diba, T.; Zheng, Q.; Solares, S. D.; Zara, J. M.; Shen, Y.; Shuai, D.; Shen, Y. Visible-Light-Responsive Photocatalyst of Graphitic Carbon Nitride for Pathogenic Biofilm Control. *ACS Appl. Mater. Interfaces* **2019**, *11*, 373−384.
(8) *Global Carbon Nitride Market Growth 2020−2025; Chemical and Material 138952*; Marketsandresearch.biz, 2020; p 132.
(9) Zhang, P.; Guo, Z.; Zhang, Z.; Fu, H.; White, J. C.; Lynch, I. Nanomaterial Transformation in the Soil−Plant System: Implications for Food Safety and Application in Agriculture. *Small* **2020**, *16*, 2000705.
(10) Lead, J. R.; Batley, G. E.; Alvarez, P. J. J.; Croteau, M.-N.; Handy, R. D.; McLaughlin, M. J.; Judy, J. D.; Schirmer, K. Nanomaterials in the Environment: Behavior, Fate, Bioavailability, and Effects-An Updated Review. *Environ. Toxicol. Chem.* **2018**, *37*, 2029−2063.
(11) Miernicki, M.; Hofmann, T.; Eisenberger, I.; von der Kammer, F.; Praetorius, A. Legal and Practical Challenges in Classifying Nanomaterials According to Regulatory Definitions. *Nat. Nanotechnol.* **2019**, *14*, 208−216.
(12) Xue, X.; Yang, J.-Y.; He, Y.; Wang, L.-R.; Liu, P.; Yu, L.-S.; Bi, G.-H.; Zhu, M.-M.; Liu, Y.-Y.; Xiang, R.-W.; Yang, X.-T.; Fan, X.-Y.; Wang, X.-M.; Qi, J.; Zhang, H.-J.; Wei, T.; Cui, W.; Ge, G.-L.; Xi, Z.-X.; Wu, C.-F.; Liang, X.-J. Aggregated Single-Walled Carbon Nanotubes Attenuate the Behavioural and Neurochemical Effects of Methamphetamine in Mice. *Nat. Nanotechnol.* **2016**, *11*, 613−620.
(13) Pomilla, F. R.; Cortes, M. A. L. R. M.; Hamilton, J. W. J.; Molinari, R.; Barbieri, G.; Marcì, G.; Palmisano, L.; Sharma, P. K.; Brown, A.; Byrne, J. A. An Investigation into the Stability of Graphitic C_3N_4 as a Photocatalyst for CO_2 Reduction. *J. Phys. Chem. C* **2018**, *122*, 28727−28738.
(14) Xiao, J.; Han, Q.; Xie, Y.; Yang, J.; Su, Q.; Chen, Y.; Cao, H. Is C_3N_4 Chemically Stable toward Reactive Oxygen Species in Sunlight-Driven Water Treatment? *Environ. Sci. Technol.* **2017**, *51*, 13380−13387.
(15) Zhang, Y.; Qiang, L.; Yuan, Y.; Wu, W.; Sun, B.; Zhu, L. Impacts of Titanium Dioxide Nanoparticles on Transformation of Silver Nanoparticles in Aquatic Environments. *Environ. Sci.: Nano* **2018**, *5*, 1191−1199.
(16) Du, T.; Adeleye, A. S.; Zhang, T.; Jiang, C.; Zhang, M.; Wang, H.; Li, Y.; Keller, A. A.; Chen, W. Influence of Light Wavelength on the Photoactivity, Physicochemical Transformation, and Fate of Graphene Oxide in Aqueous Media. *Environ. Sci.: Nano* **2018**, *5*, 2590−2603.
(17) Qu, X.; Alvarez, P. J. J.; Li, Q. Photochemical Transformation of Carboxylated Multiwalled Carbon Nanotubes: Role of Reactive Oxygen Species. *Environ. Sci. Technol.* **2013**, *47*, 14080−14088.
(18) Frank, B. P.; Sigmon, L. R.; Deline, A. R.; Lankone, R. S.; Gallagher, M. J.; Zhi, B.; Haynes, C. L.; Fairbrother, D. H. Photochemical Transformations of Carbon Dots in Aqueous Environments. *Environ. Sci. Technol.* **2020**, *54*, 4160−4170.
(19) Bai, H.; Jiang, W.; Kotchey, G. P.; Saidi, W. A.; Bythell, B. J.; Jarvis, J. M.; Marshall, A. G.; Robinson, R. A. S.; Star, A. Insight into the Mechanism of Graphene Oxide Degradation via the Photo-Fenton Reaction. *J. Phys. Chem. C* **2014**, *118*, 10519−10529.
(20) Yue, J.; Zhang, K.; Yu, H.; Yu, L.; Hou, T.; Chen, X.; Ge, H.; Hayat, T.; Alsaedi, A.; Wang, S. Mechanism Insights into Tunable Photoluminescence of Carbon Dots by Hydroxyl Radicals. *J. Mater. Sci.* **2019**, *54*, 6140−6150.
(21) Zhu, X.; Zhang, T.; Sun, Z.; Chen, H.; Guan, J.; Chen, X.; Ji, H.; Du, P.; Yang, S. Black Phosphorus Revisited: A Missing Metal-Free Elemental Photocatalyst for Visible Light Hydrogen Evolution. *Adv. Mater.* **2017**, *29*, 1605776.
(22) Parzinger, E.; Miller, B.; Blaschke, B.; Garrido, J. A.; Ager, J. W.; Holleitner, A.; Wurstbauer, U. Photocatalytic Stability of Single- and Few-Layer MoS_2. *ACS Nano* **2015**, *9*, 11302−11309.
(23) Hu, S.; Shaner, M. R.; Beardslee, J. A.; Lichterman, M.; Brunschwig, B. S.; Lewis, N. S. Amorphous TiO_2 Coatings Stabilize

Si, GaAs, and GaP Photoanodes for Efficient Water Oxidation. *Science* **2014**, *344*, 1005−1009.
(24) Mashtalir, O.; Cook, K. M.; Mochalin, V. N.; Crowe, M.; Barsoum, M. W.; Gogotsi, Y. Dye Adsorption and Decomposition on Two-Dimensional Titanium Carbide in Aqueous Media. *J. Mater. Chem. A* **2014**, *2*, 14334−14338.
(25) Niu, P.; Zhang, L.; Liu, G.; Cheng, H.-M. Graphene-Like Carbon Nitride Nanosheets for Improved Photocatalytic Activities. *Adv. Funct. Mater.* **2012**, *22*, 4763−4770.
(26) Xiao, Y.; Tian, G.; Li, W.; Xie, Y.; Jiang, B.; Tian, C.; Zhao, D.; Fu, H. Molecule Self-Assembly Synthesis of Porous Few-Layer Carbon Nitride for Highly Efficient Photoredox Catalysis. *J. Am. Chem. Soc.* **2019**, *141*, 2508−2515.
(27) Chen, C.-Y.; Jafvert, C. T. Photoreactivity of Carboxylated Single-Walled Carbon Nanotubes in Sunlight: Reactive Oxygen Species Production in Water. *Environ. Sci. Technol.* **2010**, *44*, 6674−6679.
(28) Song, Z.; Wang, M.; Wang, Z.; Wang, Y.; Li, R.; Zhang, Y.; Liu, C.; Liu, Y.; Xu, B.; Qi, F. Insights into Heteroatom-Doped Graphene for Catalytic Ozonation: Active Centers, Reactive Oxygen Species Evolution, and Catalytic Mechanism. *Environ. Sci. Technol.* **2019**, *53*, 5337−5348.
(29) Maezono, T.; Tokumura, M.; Sekine, M.; Kawase, Y. Hydroxyl Radical Concentration Profile in Photo-Fenton Oxidation Process: Generation and Consumption of Hydroxyl Radicals during the Discoloration of Azo-Dye Orange II. *Chemosphere* **2011**, *82*, 1422−1430.
(30) Kwan, W. P.; Voelker, B. M. Rates of Hydroxyl Radical Generation and Organic Compound Oxidation in Mineral-Catalyzed Fenton-like Systems. *Environ. Sci. Technol.* **2003**, *37*, 1150−1158.
(31) Jothinathan, L.; Hu, J. Kinetic Evaluation of Graphene Oxide Based Heterogenous Catalytic Ozonation for the Removal of Ibuprofen. *Water Res.* **2018**, *134*, 63−73.
(32) Park, J.-S.; Choi, H.; Cho, J. Kinetic Decomposition of Ozone and Para-Chlorobenzoic Acid (p-CBA) during Catalytic Ozonation. *Water Res.* **2004**, *38*, 2285−2292.
(33) Yoon, Y.; Moon, J.; Kwon, M.; Jung, Y.; Kim, S.; Kang, J.-W. Evaluation of the Catalytic Effect of the Ozone/Carbon Nanotube (O_3/CNT) Process Using Para-Chlorobenzoic Acid (p-CBA). *Ozone: Sci. Eng.* **2014**, *36*, 465−471.
(34) Xiao, J.; Xie, Y.; Cao, H.; Wang, Y.; Guo, Z.; Chen, Y. Towards Effective Design of Active Nanocarbon Materials for Integrating Visible-Light Photocatalysis with Ozonation. *Carbon* **2016**, *107*, 658−666.
(35) VandeVondele, J.; Krack, M.; Mohamed, F.; Parrinello, M.; Chassaing, T.; Hutter, J. Quickstep: Fast and Accurate Density Functional Calculations Using a Mixed Gaussian and Plane Waves Approach. *Comput. Phys. Commun.* **2005**, *167*, 103−128.
(36) Goedecker, S.; Teter, M.; Hutter, J. Separable Dual-Space Gaussian Pseudopotentials. *Phys. Rev. B: Condens. Matter Mater. Phys.* **1996**, *54*, 1703−1710.
(37) Krukau, A. V.; Vydrov, O. A.; Izmaylov, A. F.; Scuseria, G. E. Influence of the Exchange Screening Parameter on the Performance of Screened Hybrid Functionals. *J. Chem. Phys.* **2006**, *125*, 224106.
(38) Woon, D. E.; Dunning, T. H. Gaussian Basis Sets for Use in Correlated Molecular Calculations. IV. Calculation of Static Electrical Response Properties. *J. Chem. Phys.* **1994**, *100*, 2975−2988.
(39) Genovese, L.; Deutsch, T.; Goedecker, S. Efficient and Accurate Three-Dimensional Poisson Solver for Surface Problems. *J. Chem. Phys.* **2007**, *127*, 054704.
(40) Zhao, H.; Yu, H.; Quan, X.; Chen, S.; Zhao, H.; Wang, H. Atomic Single Layer Graphitic-C_3N_4: Fabrication and Its High Photocatalytic Performance under Visible Light Irradiation. *RSC Adv.* **2014**, *4*, 624−628.
(41) Xiao, J.; Xie, Y.; Rabeah, J.; Brückner, A.; Cao, H. Visible-Light Photocatalytic Ozonation Using Graphitic C_3N_4 Catalysts: A Hydroxyl Radical Manufacturer for Wastewater Treatment. *Acc. Chem. Res.* **2020**, *53*, 1024−1033.
(42) Lan, H.; Wang, F.; Lan, M.; An, X.; Liu, H.; Qu, J. Hydrogen-Bond-Mediated Self-Assembly of Carbon-Nitride-Based Photo-Fenton-like Membranes for Wastewater Treatment. *Environ. Sci. Technol.* **2019**, *53*, 6981−6988.
(43) Yi, F.; Gan, H.; Jin, H.; Zhao, W.; Zhang, K.; Jin, H.; Zhang, H.; Qian, Y.; Ma, J. Sulfur- and Chlorine-Co-Doped g-C_3N_4 Nanosheets with Enhanced Active Species Generation for Boosting Visible-Light Photodegradation Activity. *Sep. Purif. Technol.* **2020**, *233*, 115997.
(44) Wang, G.; Zhang, T.; Yu, W.; Si, R.; Liu, Y.; Zhao, Z. Modulating Location of Single Copper Atoms in Polymeric Carbon Nitride for Enhanced Photoredox Catalysis. *ACS Catal.* **2020**, *10*, 5715−5722.
(45) Zheng, Q.; Xu, E.; Park, E.; Chen, H.; Shuai, D. Looking at the Overlooked Hole Oxidation: Photocatalytic Transformation of Organic Contaminants on Graphitic Carbon Nitride under Visible Light Irradiation. *Appl. Catal., B* **2019**, *240*, 262−269.
(46) Zheng, Q.; Durkin, D. P.; Elenewski, J. E.; Sun, Y.; Banek, N. A.; Hua, L.; Chen, H.; Wagner, M. J.; Zhang, W.; Shuai, D. Visible-Light-Responsive Graphitic Carbon Nitride: Rational Design and Photocatalytic Applications for Water Treatment. *Environ. Sci. Technol.* **2016**, *50*, 12938−12948.
(47) Alrousan, D. M. A.; Dunlop, P. S. M. Evaluation of Ozone-Based Oxidation and Solar Advanced Oxidation Treatment of Greywater. *J. Environ. Chem. Eng.* **2020**, *8*, 104309.
(48) Hirakawa, T.; Nosaka, Y. Properties of $O_2^{\cdot-}$ and $OH^{\cdot}$ Formed in TiO_2 Aqueous Suspensions by Photocatalytic Reaction and the Influence of H_2O_2 and Some Ions. *Langmuir* **2002**, *18*, 3247−3254.
(49) Takeuchi, N.; Mizoguchi, H. Study of Optimal Parameters of the H_2O_2/O_3 Method for the Decomposition of Acetic Acid. *Chem. Eng. J.* **2017**, *313*, 309−316.
(50) Ma, H.; Zhang, X.; Jin, F.; Zhou, H.; Zhang, J.; Ma, Y. Crucial Roles of Triazinic-N=O and C=O Groups in Photocatalytic Water Splitting on Graphitic Carbon Nitride. *J. Mater. Chem. A* **2021**, *9*, 5522−5532.
(51) Chen, P.; Zhou, T.; Xing, L.; Xu, K.; Tong, Y.; Xie, H.; Zhang, L.; Yan, W.; Chu, W.; Wu, C.; Xie, Y. Atomically Dispersed Iron-Nitrogen Species as Electrocatalysts for Bifunctional Oxygen Evolution and Reduction Reactions. *Angew. Chem., Int. Ed.* **2017**, *56*, 610−614.
(52) Herrera, F.; Owrutsky, J. Molecular Polaritons for Controlling Chemistry with Quantum Optics. *J. Chem. Phys.* **2020**, *152*, 100902.
(53) Ehrmaier, J.; Domcke, W.; Opalka, D. Mechanism of Photocatalytic Water Oxidation by Graphitic Carbon Nitride. *J. Phys. Chem. Lett.* **2018**, *9*, 4695−4699.
(54) Tijani, J. O.; Babajide, O. O.; Petrik, L. F.; Petrik, F. Pharmaceuticals, Endocrine Disruptor, Personal Care Products, Nanomaterials and Perfluorinated Pollutants: A Review. *Environ. Chem. Lett.* **2016**, *14*, 27−49.
(55) Asif, M. B.; Nguyen, L. N.; Price, W. E.; Nghiem, L. D.; Nghiem, D. Integration of an Enzymatic Bioreactor with Membrane Distillation for Enhanced Biodegradation of Trace Organic Contaminants. *Int. Biodeterior. Biodegrad.* **2017**, *124*, 73−81.
(56) Jiang, L.; Yuan, X.; Pan, Y.; Liang, J.; Zeng, G.; Wu, Z.; Wang, H. Doping of Graphitic Carbon Nitride for Photocatalysis: A Reveiw. *Appl. Catal., B* **2017**, *217*, 388−406.
(57) Zheng, X.; Zhang, Q.; Chen, T.; Wu, Y.; Hao, J.; Tan, C.; Chen, P.; Wang, F.; Liu, H.; Lv, W.; Liu, G. A Novel Synthetic Carbon and Oxygen Doped Stalactite-like g-C_3N_4 for Broad-Spectrum-Driven Indometacin Degradation. *J. Hazard. Mater.* **2020**, *386*, 121961.
(58) Minero, C.; Chiron, S.; Falletti, G.; Maurino, V.; Pelizzetti, E.; Ajassa, R.; Carlotti, M. E.; Vione, D. Photochemincal Processes Involving Nitrite in Surface Water Samples. *Aquat. Sci.* **2007**, *69*, 71−85.
(59) Vione, D.; Falletti, G.; Maurino, V.; Minero, C.; Pelizzetti, E.; Malandrino, M.; Ajassa, R.; Olariu, R.-I.; Arsene, C. Sources and Sinks of Hydroxyl Radicals upon Irradiation of Natural Water Samples. *Environ. Sci. Technol.* **2006**, *40*, 3775−3781.

https://doi.org/10.1021/acs.est.1c03804
Environ. Sci. Technol. 2021, 55, 12414−12423

(60) Mopper, K.; Zhou, X. Hydroxyl Radical Photoproduction in the Sea and Its Potential Impact on Marine Processes. *Science* **1990**, *250*, 661−664.
(61) Minella, M.; De Laurentiis, E.; Maurino, V.; Minero, C.; Vione, D. Dark Production of Hydroxyl Radicals by Aeration of Anoxic Lake Water. *Sci. Total Environ.* **2015**, *527*−*528*, 322−327.
(62) Liao, P.; Yu, K.; Lu, Y.; Wang, P.; Liang, Y.; Shi, Z. Extensive Dark Production of Hydroxyl Radicals from Oxygenation of Polluted River Sediments. *Chem. Eng. J.* **2019**, *368*, 700−709.
(63) Page, S. E.; Kling, G. W.; Sander, M.; Harrold, K. H.; Logan, J. R.; McNeill, K.; Cory, R. M. Dark Formation of Hydroxyl Radical in Arctic Soil and Surface Waters. *Environ. Sci. Technol.* **2013**, *47*, 12860−12867.

https://doi.org/10.1021/acs.est.1c03804
Environ. Sci. Technol. 2021, 55, 12414−12423